


Cite this: *J. Mater. Chem. A*, 2021, 9, 11381

# Structural engineering of metal–organic framework derived tin sulfides for advanced Li/Na storage†

Qiaohuan Cheng and Xuebin Yu \*

Tin sulfides have attracted considerable attention due to their unique layered structure, large interlayer spacing and high theoretical capacity for both lithium-ion batteries (LIBs) and sodium-ion batteries (NIBs). However, the development of tin sulfides has been limited by their poor rate capability and cycle life. To intrinsically maximize the lithium/sodium storage properties of tin sulfides, herein, a metal–organic framework (MOF) template-based strategy is developed to fabricate SnS<sub>2</sub>@C and SnS@C for LIBs, as well as 3D hollow rod-like SnS@nitrogen-doped carbon@nitrogen-doped graphene (SnS@NC@NG) to accommodate Na<sup>+</sup> behavior in NIBs. The results show that structural/physicochemical characterization helps gain insights into the intrinsic relationships between the sulfidation temperature and crystal structures as well as lithium/sodium storage behaviors. The as-prepared SnS<sub>2</sub>@C and SnS@C exhibit superior Li<sup>+</sup> storage behavior to SnS<sub>x</sub>-based electrodes benefiting from their unique structures (798.3 mA h g<sup>-1</sup> and 850.9 mA h g<sup>-1</sup> at 5 A g<sup>-1</sup> after 4000 and 5000 cycles, respectively). Particularly, the resulting SnS@NC@NG demonstrates a robust 3D hollow interacted nanostructure during sodiation/desodiation processes, showing ultrahigh specific capacity, rate capability and excellent cycle lifetimes (501.5 mA h g<sup>-1</sup> at 2.0 A g<sup>-1</sup> after 5000 cycles). This work presents a newly effective strategy to construct high-performance tin sulfide hybrids for energy storage.

Received 1st March 2021  
Accepted 15th April 2021

DOI: 10.1039/d1ta01768c

rsc.li/materials-a

## Introduction

Since the energy density and charging/discharging rate of batteries are key factors in determining the power of mechanical and electronic devices, extensive investigations have been performed on high-rate electrode materials and various battery systems.<sup>1,2</sup> Nowadays, lithium-ion batteries (LIBs) still play a dominant role in renewable energy storage owing to their high energy density and output voltage.<sup>3</sup> However, the ever-increasing consumption and rarity of lithium raw materials will hinder their larger scale applications in the future. Recently, alternative rechargeable Na-ion batteries (NIBs) have received significant attention in virtue of the high relative abundance and low-cost of Na<sup>+</sup> along with them showing similar rocking chair mechanisms to LIBs and possessing high energy density due to the closely standard reduction potential between lithium and sodium (−2.71 Å and −3.04 Å vs. the standard hydrogen electrode, respectively).<sup>5–7</sup> Therefore, rechargeable LIBs and NIBs are mutually complementary and suitable for different applications.<sup>8</sup> However, it should be noted that it is still a great challenge to obtain suitable anode

materials for both LIBs and NIBs, which determine the full cell performance compared with cathode materials.<sup>9</sup> Taking the graphite anode for example, which is a state-of-the-art anode material for commercial LIBs, it was found that it only shows a very low capacity of less than 35 mA h g<sup>-1</sup> for NIBs.<sup>10</sup>

This is due to the fact that Na<sup>+</sup> with a much larger ionic radius than Li<sup>+</sup> (1.02 Å and 0.76 Å, respectively) always leads to sluggish kinetics and huge volumetric expansion of electrodes.<sup>11,12</sup> Thus, it is difficult to adapt anodes for Li-based systems to NIBs directly to satisfy two different battery systems. In this regard, great efforts have been dedicated to exploring and constructing available anodes for LIBs and NIBs with a moderate voltage platform, high power density and long cycling life.

Recently, transition-metal sulfide (TMS) based electrodes, such as Fe<sub>x</sub>S, Co<sub>x</sub>S, Cu<sub>x</sub>S and SnS<sub>x</sub> have drawn tremendous attention owing to their high theoretical capacity and excellent redox reversibility; besides the weaker bonding of metal–sulfur enhances the reversibility of the conversion reaction during cycling more than that of oxide counterparts.<sup>13–15</sup> In particular, tin sulfides existing in two stable forms: SnS<sub>2</sub> and SnS have been widely researched as host materials for Li/Na ion storages because of their high theoretical capacity, in which SnS/SnS<sub>2</sub> can deliver 1137/1232 mA h g<sup>-1</sup> for LIBs and 1022/1136 mA h g<sup>-1</sup> for NIBs in theory, respectively, through a combined electrochemical conversion and alloying

Department of Materials Science, Fudan University, Shanghai 200433, China. E-mail: yuxuebin@fudan.edu.cn

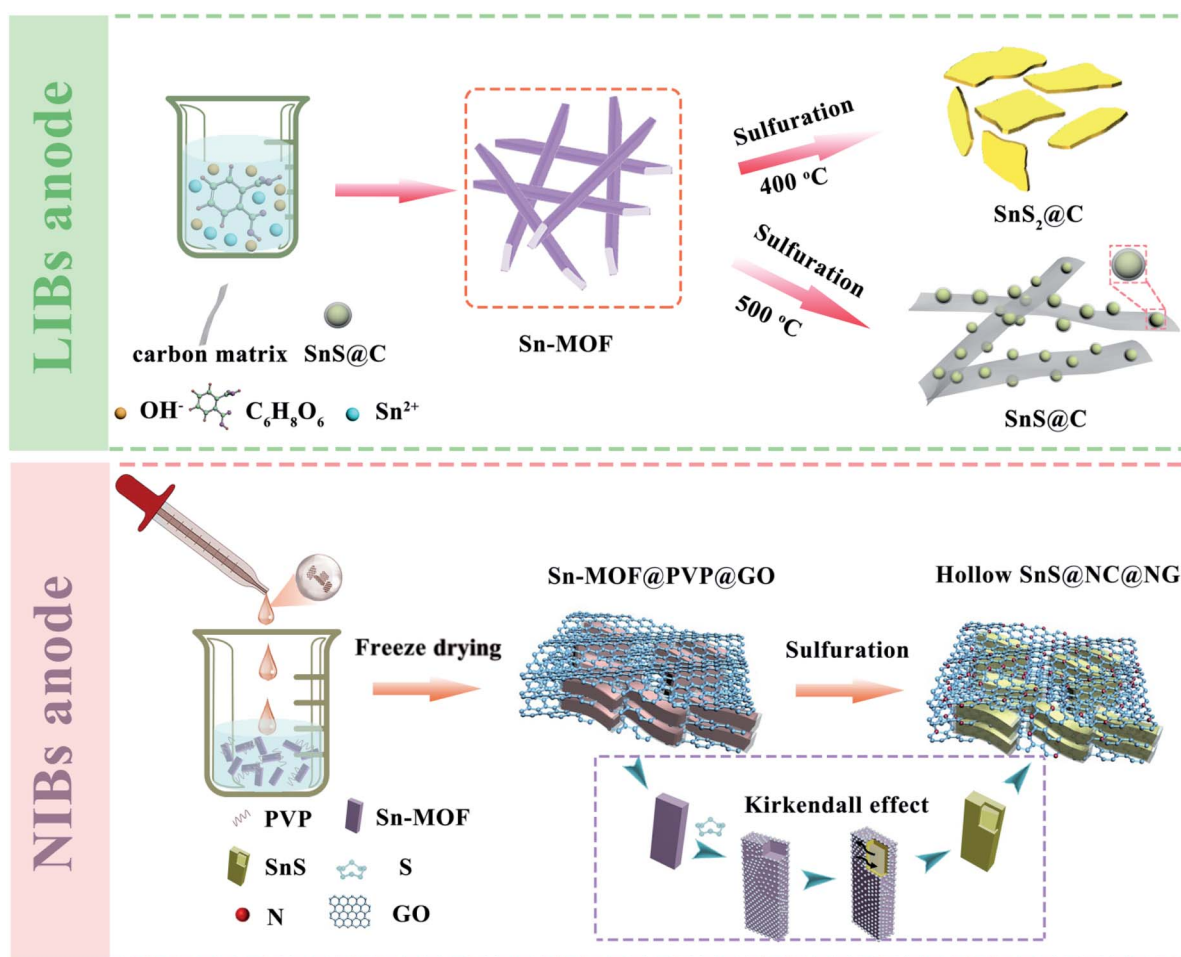
† Electronic supplementary information (ESI) available. See DOI: 10.1039/d1ta01768c

mechanisms.<sup>16,17</sup> In addition, the large interlayer can be of assistance to reversibly insert and extract  $\text{Na}^+/\text{Li}^+$  (5.9 Å and 4.33 Å for  $\text{SnS}_2$  and  $\text{SnS}$ , respectively, vs. 1.02 Å for  $\text{Na}^+$  and 0.76 Å for  $\text{Li}^+$ ).<sup>18,19</sup> As a result, tin sulfides can be highly regarded as promising host materials for Li/Na ion storage. And it is noteworthy that  $\text{SnS}$  shows more suitable properties to accommodate the complicated electrochemical reactions between the electrode and Na ions compared with  $\text{SnS}_2$ . For example, it has small lattice expansion during the sodiation/desodiation processes (242% for  $\text{SnS}$  and 324% for  $\text{SnS}_2$ ), and only undergoes a two-structure transformation compared with the three-structure phase reaction in  $\text{SnS}_2$ .<sup>20,21</sup>

Unfortunately, bulk tin sulfides suffer from low conductivity, sluggish kinetics and severe pulverization during the cycling process, which seriously limit their ultimate electrochemical behavior for both LIBs and NIBs.<sup>22,23</sup> Accordingly, it has been demonstrated that the rational design of materials with a favorable structure and morphology through combined nanostructured  $\text{SnS}$  ( $\text{SnS}_2$ ) with conductive substrates (graphene, carbonaceous materials, conductive polymers *etc.*) can be an effective approach to boost lithium/sodium storage properties.<sup>19,24–26</sup> Appealingly, metal–organic frameworks (MOFs) composed of metal ions/clusters and organic ligands

have been demonstrated to be promising precursors/templates for fabricating metal sulfides/carbon composites with a unique and highly controllable structure.<sup>27,28</sup> Most strikingly, the carbonized and graphitized carbon derived from organic ligands can *in situ* fully encapsulate the active metal sulfides during the simultaneous decomposition and sulfidation of a preformed MOF.<sup>29</sup> In particular it is noteworthy that the Kirkendall effect always comes along with the sulfidation process, which triggers hollow structures to form in the precursors during this process.<sup>30</sup> Hence, MOF-derived metal sulfides/carbon composites can deliver superior electrochemical behavior in virtue of greatly improved electronic conductivity/ion diffusion, and remaining electrode integrity.

In this paper,  $\text{SnS}_2@\text{C}$ ,  $\text{SnS}@\text{C}$  and  $\text{SnS}@\text{nitrogen-doped carbon}@\text{nitrogen-doped reduced graphene oxide}$  ( $\text{SnS}@\text{NC}@\text{NG}$ ) composites are synthesized with a Sn-based MOF precursor for the storage of Li and Na ions, respectively. The unique  $\text{SnS}_2@\text{C}$  nanoplate and  $\text{SnS}@\text{C}$  composites exhibit large reversible capacities, excellent rate performances and stable cycling behaviors when utilized as anode materials for LIBs, in which the  $\text{SnS}_2@\text{C}$  nanoplate delivers a reversible capacity of 798.3  $\text{mA h g}^{-1}$  at 5  $\text{A g}^{-1}$  after 4000 cycles, and  $\text{SnS}@\text{C}$  delivers a higher capacity of 850.9  $\text{mA h g}^{-1}$  at 5  $\text{A g}^{-1}$

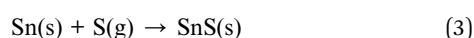
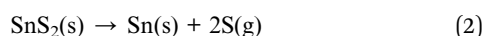
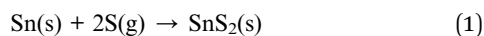


Scheme 1 Schematic illustration of the fabrication process of  $\text{SnS}_2@\text{C}$ ,  $\text{SnS}@\text{C}$  and  $\text{SnS}@\text{NC}@\text{NG}$ .

after a long-term lifetime over 5000 cycles. To alleviate the big volumetric expansion and promote electrode stabilities for NIBs, we then rationally design a smart SnS@NC@NG hybrid structure with superior sodium storage behavior, in which hollow rod-like SnS@NC composites are sandwiched within N-doped rGO in virtue of the Kirkendall effect and the assistance of PVP (polyvinyl pyrrolidone) during the sulfidation of MOF precursors. As a result, the SnS@NC@NG composites deliver a superior long cycling stability with a capacity of 501.5 mA h g<sup>-1</sup> after 5000 cycles at 2.0 A g<sup>-1</sup> and good rate performances with 605.6 mA h g<sup>-1</sup> and 558.0 mA h g<sup>-1</sup> at 5 A g<sup>-1</sup> and 10 A g<sup>-1</sup>, respectively. This work provides an effective route toward constructing SnS<sub>2</sub>/SnS-based anode materials with superior electrochemical performances for lithium and sodium storage.

## Results and discussion

The typical synthesis procedure of SnS<sub>2</sub>@C, SnS@C and SnS@NC@NG composites is illustrated in Scheme 1. The Sn-based MOF was synthesized through a wet chemistry process with *o*-phthalic acid (C<sub>8</sub>H<sub>6</sub>O<sub>4</sub>) as an organic linker.<sup>31</sup> It is noteworthy that the deprotonation of *o*-phthalic acid after addition of NaOH could be easy to link with Sn<sup>2+</sup> to form a 1D rectangular rod composite, Sn-MOF. In the following sulfuration process, the Sn-MOF was converted to SnS<sub>2</sub>@C and SnS@C composites *via* the simultaneous decomposition and solid-gas reaction with sulfur powders at different sulfuration temperature with flowing argon gas, respectively. At a low sulfuration temperature of 400 °C, the central coordination tin-ions are *in situ* transformed into SnS<sub>2</sub>, and the 1D rod-like MOF precursors crack into several pieces due to the big tension during the formation of SnS<sub>2</sub>. When the temperature is increased up to 500 °C, we propose that the SnS phase derived from Sn precursors and S powder may be interpreted as the result of the associated reaction defined as follows:<sup>32</sup>



At a high temperature, the SnS<sub>2</sub> phase formed at a low temperature is dissociated into Sn(s) and S(g) quickly, then Sn(s) reacts with S(g) to form SnS particles due to the low melting point of Sn (232 °C), which tends to evaporate to form beads at high temperatures, along with the carbonization of organic ligands into amorphous carbon. For SnS@NC@NG, we ingeniously design it to accommodate the long-term sodiation/desodiation behaviors. Firstly, GO aqueous dispersion was dropped slowly into the solution mixture of the Sn-MOF and PVP. During this process, the chemically modified MOFs with functional groups, in which amide carbonyl groups of PVP can coordinate with metal ions (Sn) of MOFs, achieve a uniform distribution on GO through the coordination interaction

between amide carbonyl groups of the modified MOF and GO.<sup>33–35</sup> Secondly, after the freeze drying process, the functionalized GO sheets assembled into a 3D coherent network structure. Subsequently, the Sn-MOF@PVP@GO composites were converted to hollow rod-like SnS@NC@NG composites *via* a sulfuration process accompanied by carbonization. Specially, the unique hollow rod-like structure can be attributed to the Kirkendall effects, and the unbalance diffusion rate between Sn and S where the Sn diffuses outward faster than S does inward, which makes the SnS grow against the inner rod wall, finally leading to a hollow structure.<sup>30,36</sup> In addition, the GO was reduced to NG since the N-source was provided by PVP.

Scanning electron microscopy (SEM) and transmission electron microscopy (TEM) observations were performed to reveal the detailed morphology and structure of the Sn-MOF and MOF-derived sulfide composite anode materials. As shown in Fig. 1a, the SEM image reveals that the obtained 1D rectangular rod-like Sn-MOF exhibits a smooth surface with a diameter of ~100 nm, and further examination shown in Fig. 1b and c demonstrate that the MOF is solid. Fig. 1d reveals that the SnS<sub>2</sub>@C composites are relatively uniform and consist of nanoplates with an irregular edge, which is a significant difference in morphology from the Sn-MOF precursor. Besides, the thickness of the randomly and disorderly distributed nanoplates with a smooth surface is about 20–50 nm (inset of Fig. 1d). A typical TEM image of SnS<sub>2</sub>@C (Fig. 1e) shows that the mono-lamellar structures stack randomly, which is in good agreement with the SEM results. The high-resolution TEM (HRTEM) image in Fig. 1f clearly shows that a nanoplate consists of only one integrated crystal particle, and the inset shows the well-crystallized SnS<sub>2</sub> with a lattice fringe of 0.27 nm, corresponding to the (101) crystalline plane. The carbon matrix coating layer is negligible. The STEM image shows the continuous bright dots within nanoplates, revealing a highly integrated crystal plate, coinciding with the SEM and TEM results. The elemental mapping analysis (Fig. 1m) evidences the coexistence of Sn, and S elements with homogeneous dispersion, while the C element was present with few bright dots distributed sporadically, indicating the low carbon content. It is believed that the mono-lamellar structure facilitates more lithium ion insertion, and the nanoplates with a large lateral size significantly enhance electron and lithium ion transport. For the SnS@C composite, as manifested in the SEM image (Fig. 1g), the nanobelt with a rough surface is evident, and the thickness of the obtained nanobelt is about 10 nm. Closer examination demonstrates that the small particles anchor firmly on the nanobelts (inset of Fig. 1g), which can be further visualized by the TEM image (Fig. 1h). As noted, the nanobelts constructed from amorphous carbon are decorated with evenly distributed SnS nanoparticles with the diameter of ~10 nm. The HRTEM image (Fig. 1i) further demonstrates that the SnS nanoparticles with a well-defined lattice fringe are tightly encapsulated by the carbon matrix, which derives from the organic linkers of MOFs. The lattice fringe of 0.23 nm is consistent with the (131) plane of SnS (inset of 1i). Furthermore, the STEM image and the elemental mapping images of Sn, S and C provide more evidence for the uniform distribution of

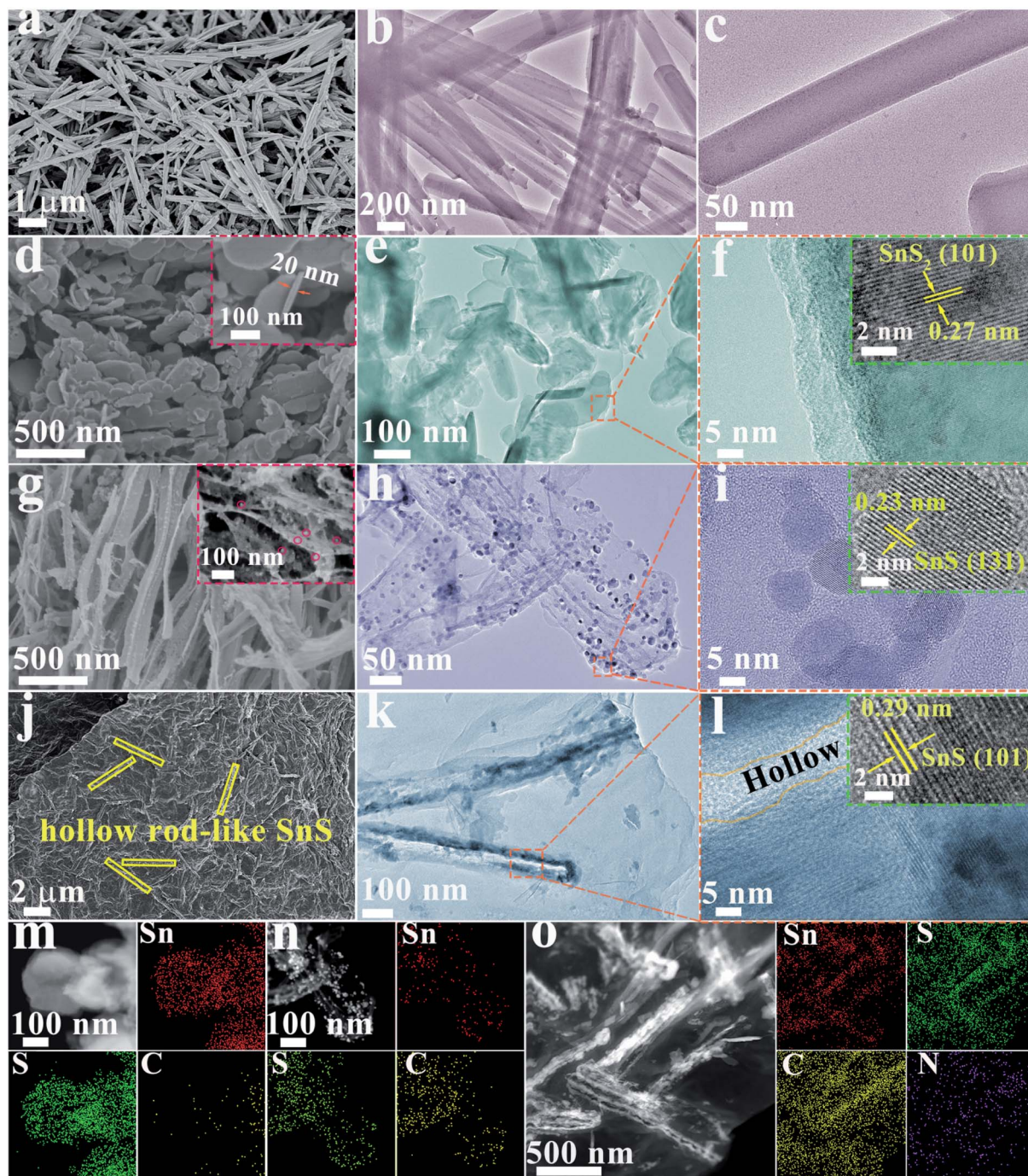


**Fig. 1** Morphology characterization of Sn-MOF, SnS<sub>2</sub>@C, SnS@C and SnS@NC@NG. (a) SEM image and (b), and (c) TEM image of Sn-MOF. (d) SEM image, (e) TEM image, (f) HRTEM image, (m) STEM image and the elemental mappings of SnS<sub>2</sub>@C. The insets of (d) and (f) show the SEM and HRTEM images of SnS<sub>2</sub>@C, respectively. (g) SEM image, (h) TEM image, (i) HRTEM image and (n) STEM image and the elemental mappings of SnS@C. The insets of (g) and (i) show the SEM and HRTEM images of SnS@C, respectively. (j) SEM image, (k) TEM image, (l) HRTEM image and (o) STEM image and the elemental mappings of SnS@NC@NG. The inset of (l) shows the HRETEM image of SnS@NC@NG.

SnS nanoparticles throughout the nanobelt (Fig. 1n). Such a unique structure of the nanobelt decorated with carbon-coated SnS nanoparticles interlaces with each other is expected to provide a convenient path for ionic and electronic transportation and suppress the agglomeration of SnS nanoparticles during the lithiation/delithiation process accounting

for superior electrochemical behaviors. To further explore the effect of the sulfidation temperature on the structure/morphology of the product, we increase the sulfidation temperature to 600 °C; the fabrication process of SnS@C-600 °C is illustrated in Fig. S1;† the obtained SnS@C-600 °C composites pretend to inherit a morphology from the MOF precursors/

template, in which a rectangular split rod-shaped structure with abundant edges can be detected (Fig. S2a†). Furthermore, it is confirmed by TEM images (Fig. S2b and c†) that the particles agglomerate into bulk SnS, which is encapsulated in a hollow carbon shell. The HRTEM image (inset of Fig. S2c†) clearly displays lattice fringes of 0.20 nm, corresponding to the (141) planes of SnS. Besides, the STEM image and elemental mapping images of Sn, S and C provide more evidence for the bulk SnS encapsulated within the hollow rod-like carbon shell (Fig. S2d†). The well-designed SnS@NC@NG composite as the anode for NIBs exhibits well-interconnected networks, and the SnS rods are confined within the carbon matrix derived from PVP and NG layers, which seems to inherit well from the Sn-MOF precursors (Fig. 1j). Further examination reveals that the SnS rod is a hollow structure with a pore diameter of  $\sim 10$  nm and encapsulated by NC and NG (Fig. 1k and l). The HRTEM image shown in the inset of Fig. 1l confirms that SnS is well-crystallized, and the lattice fringe of 0.29 nm corresponds to the (101) plane of SnS. However, in the MOF without PVP modification, SnS@C/rGO, as shown in Fig. S3a,† the obtained SnS cannot even maintain the rod structure, which becomes small nanoparticles distributed on the rGO sheet. To further confirm the role of PVP, SnS@NC was synthesized (Fig. S3b and

c†), and it presents an obvious hollow rod structure and active materials are well confined within NC. Therefore, PVP not only provides adequate functional groups to make the MOF to achieve a uniform distribution on GO to effectively protect GO from aggregation owing to lacking adequate functional groups, but also acts as a morphology retainer to confine SnS within the capsule to keep the morphology integrity from collapsing during sulfuration.<sup>37</sup> The elemental mappings (Fig. 1o) further verify the presence of N and the uniform distribution of Sn, S, C and N. The composite with such a unique structure is deemed to be a promising anode material for storage of Na-ions by virtue of three advantages: firstly, the 3D conductive networks provide an efficient and fast transport path for electrons and ions; secondly, the hollow rod-like structure along with the N-doped rGO provides abundant active sites for strengthening Na<sup>+</sup> pseudocapacitance storage;<sup>38</sup> thirdly, the SnS confined well within the NC and NG can effectively preserve the structural integrity during cycling.

As shown in Fig. 2a, the powder X-ray diffraction (XRD) pattern demonstrates the phase-pure Sn-MOF with good crystallinity and matches well with the previous study.<sup>31</sup> The XRD pattern of SnS<sub>2</sub>@C can be successfully indexed to the 2T-type layered structure (JCPDS no. 23-0677), indicating its highly

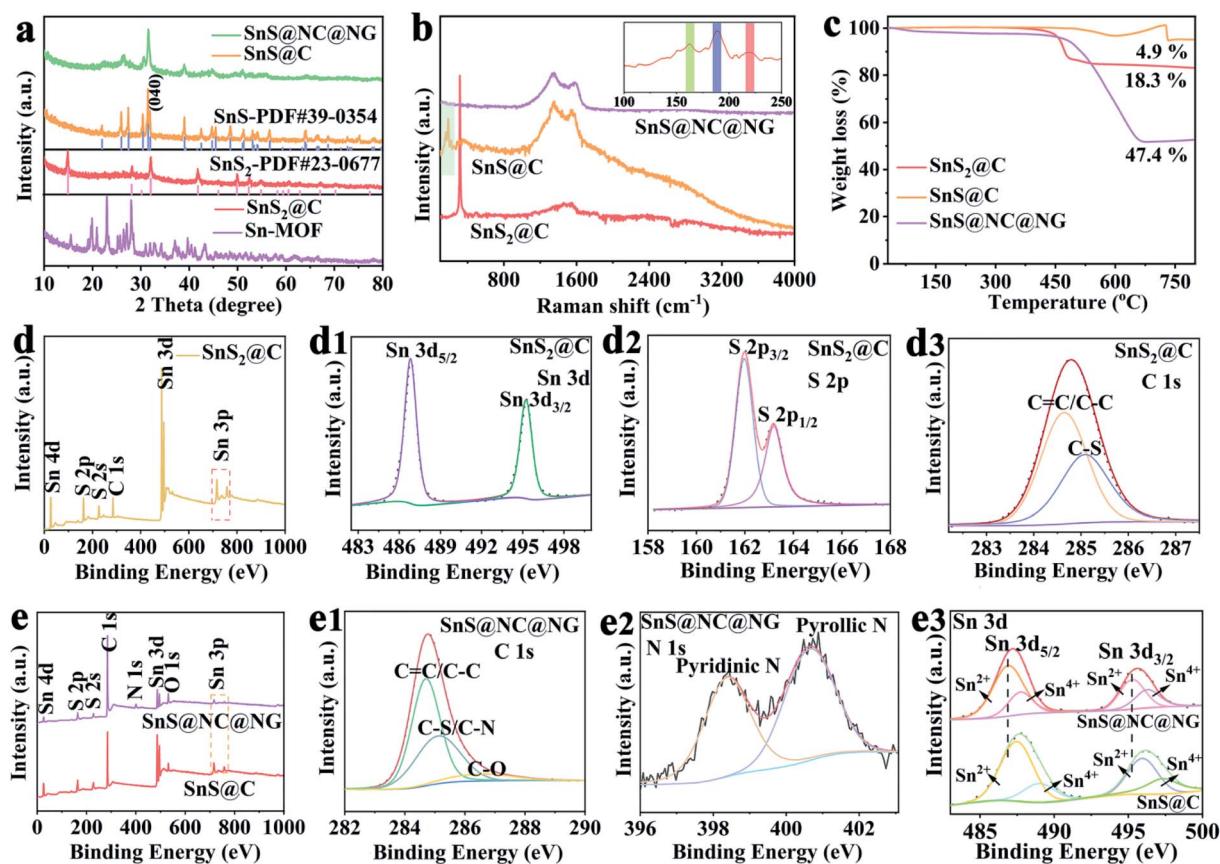


Fig. 2 (a) XRD patterns, (b) Raman spectra and (c) TGA of the SnS<sub>2</sub>@C, SnS@C and SnS@NC@NG composites, respectively. For comparison, the XRD pattern of the Sn-MOF is also presented in (a). The inset of (b) shows the enlarged Raman spectrum of SnS@C. (d) XPS survey of the SnS<sub>2</sub>@C; high-resolution spectra: (d1) Sn 3d, (d2) S 2p, and (d3) C 1s. (e) XPS survey of the SnS@C and SnS@NC@NG, respectively; high-resolution spectra: (e1) C 1s of SnS@NC@NG, (e2) N 1s of SnS@NC@NG, (e3) Sn 3d of SnS@C and SnS@NC@NG, respectively.

crystallinity and purity. For SnS@C, SnS@C-600 °C (Fig. S4†), and SnS@NC@NG, as well as the contrast samples of SnS@C/rGO and SnS@NC (Fig. S5†), all of them can be successfully indexed to orthorhombic SnS (JCPDS no. 39-0354) without impurity. Obviously, the diffraction intensities of SnS@C-600 °C are more intense and sharper than that of SnS@C, owing to the growth of crystallites and improved crystallinity with increasing temperature. Besides, the XRD peaks of SnS@NC@NG are broader than those of SnS@C, indicating that the grain size is much smaller. It is also worth noting that the (040) diffraction peak of SnS@NC@NG is almost unobservable, which can be attributed to the orientation growth of SnS in the SnS@NC@NG composites along the [010] direction being suppressed by the N-doped graphene.<sup>38</sup> There is no apparent signals for carbon or graphene, which can be attributed to the low graphitic of carbon and the great dispersion of GO originating from the synergistic effects between PVP and the MOF to avoid restacking of GO sheets during the synthesis process.<sup>39</sup>

Raman spectroscopy results also support well the structure of the hybrids (Fig. 2b). For SnS<sub>2</sub>@C, an intense peak at 315 cm<sup>-1</sup> corresponds to the A<sub>1g</sub> mode of SnS<sub>2</sub>.<sup>40,41</sup> Besides, broad humps of the G- and D-bands can be observed in SnS<sub>2</sub>@C, which is attributed to the close packed nanoplates and low content of carbon.<sup>42,43</sup> For SnS@C, three Raman shifts located at 163, 489, and 220 cm<sup>-1</sup> shown in the inset are observed, which correspond to the B<sub>3g</sub>, A<sub>g</sub> and B<sub>3u</sub> modes of SnS, respectively; moreover, the peaks of SnS@NC@NG below 250 cm<sup>-1</sup> are negligible; it can be attributed to the coverage of NC/NG.<sup>39</sup> Besides, two characteristic peaks located at ~1330 cm<sup>-1</sup> and ~1580 cm<sup>-1</sup> are observed in SnS@C and SnS@NC@NG, which correspond to the disorder/defective carbon and graphitic carbon, respectively.<sup>44,45</sup> The I<sub>D</sub>/I<sub>G</sub> values, calculated with the relative intensity of the D-band and G-band, are 1.24 and 1.05 in the order of SnS@NC@NG and SnS@C, respectively. Compared to the I<sub>D</sub>/I<sub>G</sub> value in the case of NC@NG (1.22, Fig. S6†), a higher I<sub>D</sub>/I<sub>G</sub> value for SnS@NC@NG implies that the nitrogen doped carbon and rGO possess a certain amount of defect sites, as well as the NG encapsulated rod-like SnS that increases the disorderliness of rGO, which are essential to enhance the sodium storage performance. The carbon content of the SnS<sub>2</sub>@C, SnS@C and SnS@NC@NG was investigated by thermogravimetric analysis (TGA) based on the fact that the SnS<sub>2</sub> and SnS are fully converted into SnO<sub>2</sub> at 800 °C in air (Fig. S7†). The calculated results show that the content of active materials (SnS<sub>2</sub>, SnS) is 99.1 wt%, 95.1 wt% and 52.6 wt% in SnS<sub>2</sub>@C, SnS@C and SnS@NC@NG, respectively (Fig. 2c). The higher carbon content of SnS@C-600 °C (7.6 wt%, Fig. S8†) than both SnS<sub>2</sub>@C and SnS@C indicates that the high temperature is helpful for carbon formation. The NG content in the SnS@NC@NG is determined to be 10.8 wt%, and the hybrids with different NG contents are also characterized (Fig. S9†).

X-ray photoelectron spectroscopy (XPS) tests were conducted to investigate the chemical bonding states in the SnS<sub>2</sub>@C, SnS@C and SnS@NC@NG, respectively. For SnS<sub>2</sub>@C, the full survey scan spectrum shown in Fig. 2d illustrates the presence of Sn, S and C elements. The valence of Sn ions is analyzed from the Sn 3d (Sn 3d<sub>5/2</sub> and Sn 3d<sub>3/2</sub>) spectrum (Fig. 2d1), which can

be deconvoluted into two peaks at 486.8 eV and 495.2 eV, corresponding to Sn<sup>4+</sup>.<sup>43</sup> The S peaks can be fitted into S 2p<sub>3/2</sub> (162.0 eV) and S 2p<sub>1/2</sub> (163.2 eV), which are typical signals of SnS<sub>2</sub>, suggesting the successful formation of the SnS<sub>2</sub> phase (Fig. 2d2).<sup>46</sup> The elemental C shoulder peak is exhibited in the form of C=C/C-C (284.7 eV) and C-S (285.0 eV) (Fig. 2d3).<sup>25</sup> For SnS@C and SnS@NC@NG, as shown in the full survey scan spectrum (Fig. 2e), a pronounced N 1s peak suggests the successful incorporation of the N element into the SnS@NC@NG compared with SnS@C. The low intensity of O 1s peaks for SnS@NC@NG indicates that GO is reduced to graphene by thermal treatment and most of the oxygen-functional groups in SnS@NC@NG are removed, which can also be proved in the C 1s spectrum (Fig. 2e1).<sup>39</sup> The C 1s spectrum for SnS@NC@NG can be deconvoluted into three peaks: C-C/C=C (284.7 eV), C-N/C-S (285.2 eV) and C-O (286.5 eV), which is consistent with that of NC@NG (Fig. S10a and b†).<sup>25,47</sup> The chemical state of the incorporated N is analyzed, and the high-resolution N 1s spectra in Fig. 2e2 reveal that it has two kinds of N species, pyridine N (398.4 eV) and pyrrole N (400.7 eV), which is expected to increase the electrical conductivity and the specific capacity by producing abundant defects or active sites.<sup>38</sup> Similar results can be observed in Fig. S10c† for the N 1s peak in NC@NG except for a slight shift to a lower bonding energy, suggesting that the density of electron cloud around SnS is increased after incorporation of NC@NG. For the high-resolution spectrum of Sn 3d in SnS@C and SnS@NC@NG (Fig. 2e3), there exists two peaks for Sn 3d<sub>3/2</sub> and Sn 3d<sub>5/2</sub>, respectively, which are indexed to Sn<sup>2+</sup> and Sn<sup>4+</sup>, respectively. The Sn<sup>4+</sup> in SnS@C and SnS@NC@NG can be attributed to the edges of SnS being oxidized because of the unstable state of Sn<sup>2+</sup>. Besides, the Sn 3d spectrum in SnS@NC@NG reveals a little shift toward a lower binding energy than SnS@C, indicating that the electron clouds biased from NC@NG to SnS since the systems possess electron-rich NC@NG and SnS, which is a p-type semiconductor with a large number of electron holes.<sup>38</sup> The electron clouds biased from NC@NG to SnS induce an electrostatic attraction between SnS and NC@NG, preserving the SnS detaching from the NC@NG to a certain extent during the sodiation/desodiation process and thus prolonging the cycle lifetime of NIBs.<sup>19,38,39</sup> Hence, the synergistic effects of the unique hollow structure and electrostatic attraction between SnS and NC@NG of SnS@NC@NG provides guarantees boosting of Na<sup>+</sup> storage properties.

Overall, the unique morphology of the SnS<sub>2</sub>@C nanoplate, SnS@C, in which the carbon nanobelt decorated with SnS@C nanoparticles, and hollow rod-like SnS@NC@NG composites make them potential anode materials for storage of lithium and sodium ions, respectively, and thus the corresponding electrochemical performances are investigated in detail.

As shown in Fig. 3a, the SnS<sub>2</sub>@C anode displays a good cycling stability at a current density of 100 mA g<sup>-1</sup>. It delivers an initial discharge/charge capacity of 1788.4/1238.2 mA h g<sup>-1</sup> with a coulombic efficiency of 69.32% and a high capacity retention rate of 91.11% after 100 cycles from the 2nd cycle. The low initial coulombic efficiency value can be attributed to the large amount of irreversible Li<sup>+</sup> loss in the formation of the solid-

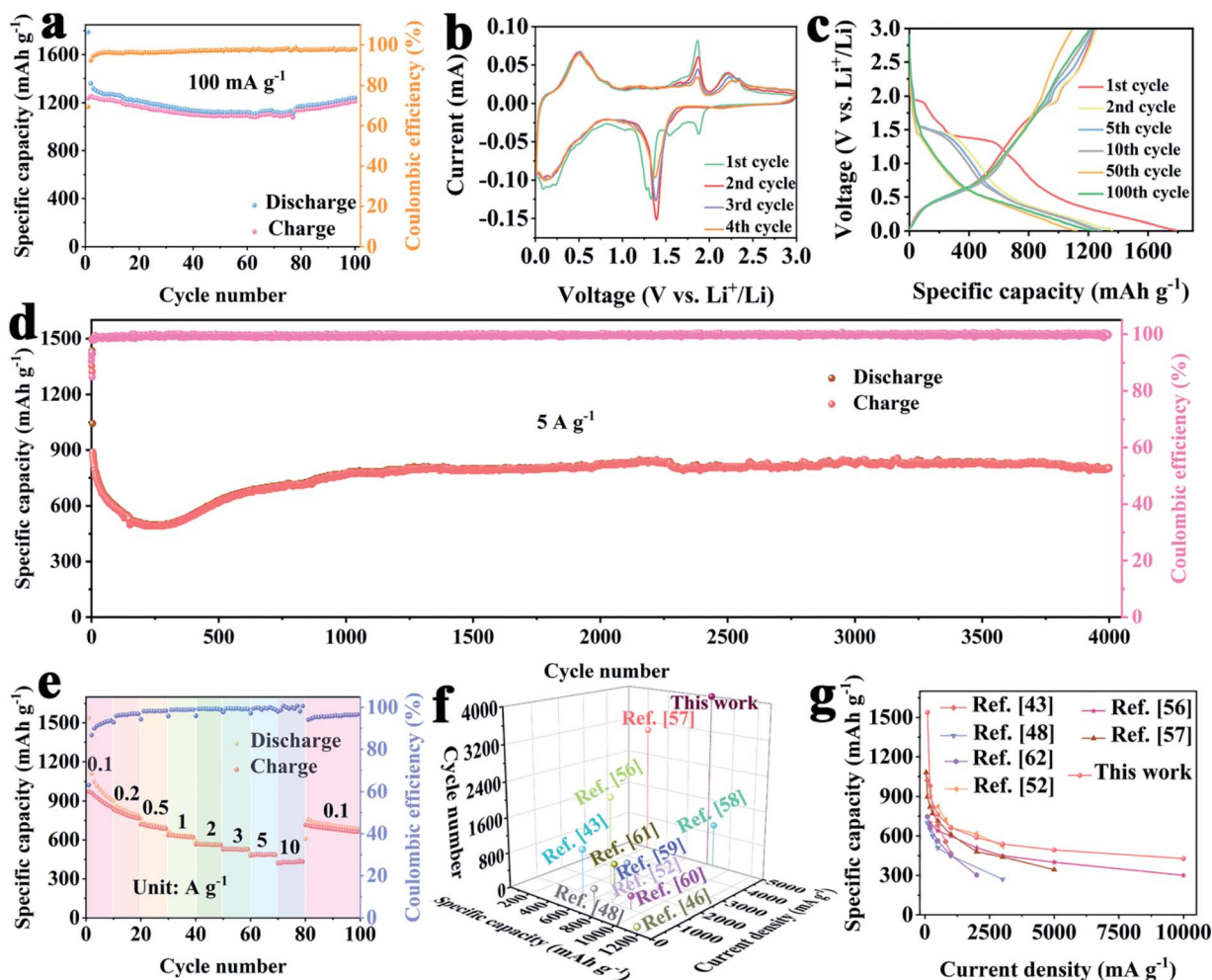
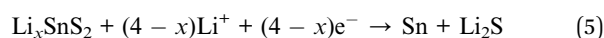
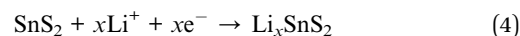
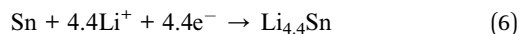


Fig. 3 Electrochemical performances of  $\text{SnS}_2\text{@C}$  for LIBs. (a) Cycling performances at a current density of  $100 \text{ mA g}^{-1}$ . (b) Cyclic voltamograms profiles at a scan rate of  $0.1 \text{ mV s}^{-1}$ . (c) Galvanostatic charge and discharge voltage profiles for the 1st, 2nd, 5th, 10th, 50th, and 100th cycles. (d) Long-term cycling behaviors along with coulombic efficiency at a current density of  $5 \text{ A g}^{-1}$ . (e) Rate performances at various current densities. Comparison of cycling performances (f) and rate capabilities (g) of  $\text{SnS}_2\text{@C}$  with those of other reported  $\text{SnS}_2$  anodes for LIBs.

electrolyte interphase (SEI). Relatively, the coulombic efficiency quickly reaches 92.24% for the 2nd cycle and exceeds 95% from the 4th cycle. Fig. 3b shows the CV measurements for the  $\text{SnS}_2\text{@C}$  at a sweep rate of  $0.1 \text{ mV s}^{-1}$  within a voltage of 0.01–3.0 V. In the first cathodic scan, the apparent peak located at 1.86 V, which disappears during the subsequent cycles, can be attributed to the lithium intercalation into the interlayers of  $\text{SnS}_2$  without phase decomposition (eqn (4)).<sup>48,49</sup> The subsequent reduction peaks at 1.32 V and 1.27 V are assigned to the conversion reaction of  $\text{Li}_x\text{SnS}_2$  to Sn and  $\text{Li}_2\text{S}$  (eqn (5)) and the formation of SEI films.<sup>49,50</sup> The peaks at 0.23 V and 0.08 V correspond to the reversible alloying process (eqn (6)).<sup>49</sup> In the first anodic scan, a peak at 0.51 V is associated with the dealloying of  $\text{Li}_x\text{Sn}$ , while another peak at 1.86 V is associated with the conversion reaction, in which Sn is oxidized at a higher potential in the charged state (eqn (7)).<sup>51,52</sup> Another apparent peak at 2.18 V corresponds to the reaction that the unreacted and dealloyed  $\text{Li}_2\text{S}$  are oxidized to polysulfides ( $2 \leq n \leq 8$ ), which is similar to Li–S batteries.<sup>49,53,54</sup> Clearly, these reversible

reactions are responsible for the high specific capacity. Fig. 3c exhibits the discharge–charge profiles of  $\text{SnS}_2\text{@C}$  at a current density of  $100 \text{ mA g}^{-1}$  for a few cycles, in which the voltage plateaus are in good accordance with the CV curves. For instance, in the first discharge profile, a voltage plateau centered at  $\sim 1.89 \text{ V}$  is assigned to lithium intercalation into the interlayers of  $\text{SnS}_2$ ; the voltage plateau located at 1.43–1.27 V corresponds to the decomposition of  $\text{Li}_x\text{SnS}_2$ . The voltage plateau shifted to a higher voltage in the subsequent discharge profiles indicating the improved kinetics after the first cycle activation. In the charge profile, the voltage plateau at about 0.5 V is attributed to the delithiation of  $\text{Li}_{4.4}\text{Sn}$ . The conversion reaction between Sn and SnS occurs at 1.89 V, and the voltage at 2.2 V should be attributed to the formation of polysulfides ( $2 \leq n \leq 8$ ) from unreacted  $\text{Li}_2\text{S}$ .





The cycle behavior of SnS<sub>2</sub>@C is evaluated at a current density of 5 A g<sup>-1</sup> (Fig. 3d), delivering a high reversible capacity of 798.3 mA h g<sup>-1</sup> after 4000 cycles. It exhibits a capacity decay in initial cycles and then a gradual increase until reaching a stable capacity. The initial capacity decay of the SnS<sub>2</sub>@C electrode can be attributed to the high mechanical/degradation resulting from the volume changes accompanying the conversion reaction as well as the formation of the unstable SEI layer.<sup>55</sup> The rising capacity after this “capacity valley” is commonly observed in various nanostructured anodes, resulting from the improved Li-diffusion kinetics caused by a high-rate lithiation-induced reactivation and the optimization of the stable SEI.<sup>6,27,55</sup>

Besides the long-term cyclability, the SnS<sub>2</sub> electrode also exhibits superior rate performance. When the current density varies from 0.1 to 10 A g<sup>-1</sup> (Fig. 3e), the SnS<sub>2</sub>@C electrode delivers reversible capacities of 1538.2, 900.1, 763.0, 664.1, 588.7, 538.5, 493.0, and 427.5 mA h g<sup>-1</sup> at various current densities of 0.1, 0.2, 0.5, 1.0, 2.0, 3.0, 5.0 and 10.0 A g<sup>-1</sup>, respectively. Clearly, the cycling and rate performance of the SnS<sub>2</sub>@C electrode are superior to those of the SnS<sub>2</sub>-based composite reported before, as shown in Fig. 3f and g.<sup>43,46,48,52,56–62</sup>

The electrochemical performances of SnS@C as LIB electrodes are also evaluated. Fig. 4a shows the cycling performances of SnS@C at a current density of 100 mA g<sup>-1</sup> at a voltage of 0.01–3.0 V. It delivers the first discharge capacity of 1660.9 mA h g<sup>-1</sup> and a reversible charge capacity of 1391.9 mA h g<sup>-1</sup> with an initial coulombic efficiency of 83.3%. And then the subsequent coulombic efficiency quickly reaches over 93% from the 2nd cycle and exceeds 95% from the 3rd cycle, indicating

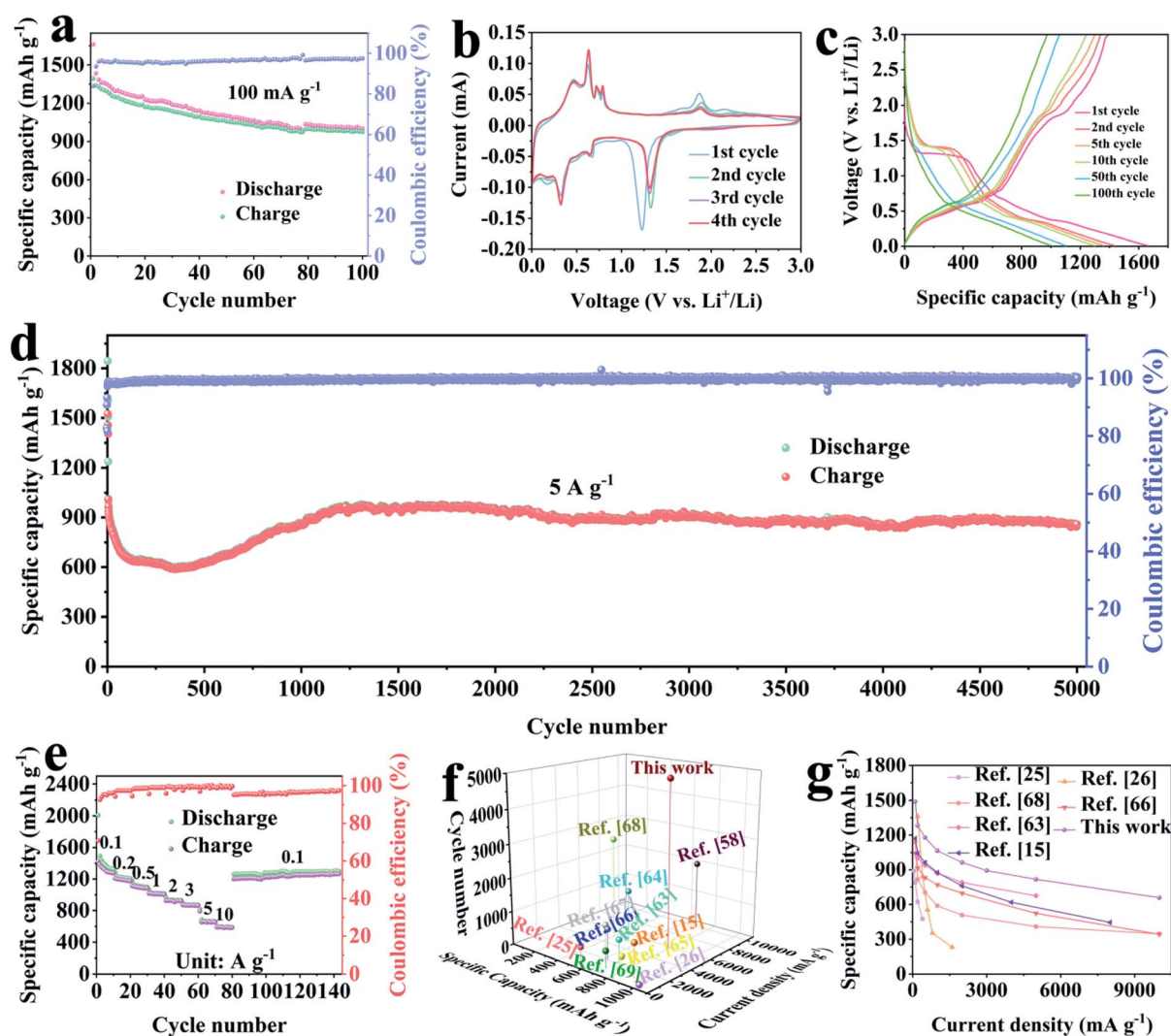
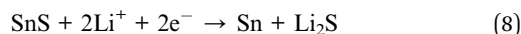


Fig. 4 Electrochemical performances of SnS@C for LIBs. (a) Cycling performances at a current density of 100 mA g<sup>-1</sup>. (b) Cyclic voltammograms profiles at a scan rate of 0.1 mV s<sup>-1</sup>. (c) Galvanostatic charge and discharge voltage profiles for the 1st, 2nd, 5th, 10th, 50th, and 100th cycles. (d) Long-term cycling behaviors along with coulombic efficiency at a current density of 5 A g<sup>-1</sup>. (e) Rate performance at various current densities. Comparison of cycling performance (f) and rate capabilities (g) of SnS@C with those of other reported SnS anodes for LIBs.



superior reversibility. After 100 cycles, the SnS@C electrode still maintains a high discharge capacity of 1001.4 mA h g<sup>-1</sup>. The CV results in Fig. 4b show that in the first cathodic scan, a prominent peak at 1.22 V corresponds to the conversion reaction between SnS and Li, which is in accordance with eqn (8).



Furthermore, the formation of the SEI layer can also be assigned to this potential, which should be responsible for a reversible capacity loss during the first discharge/charge cycle.<sup>63</sup> Obviously, the peak is positively shifted to a higher potential from the 2nd cycle, which can be attributed to the improved electrochemical kinetics after the first cycle activation. The subsequent peaks at 0.67 V, 0.33 V and 0.16 V are related to the multi-step alloying reaction between the reduced Sn and Li, as expressed in eqn (6).<sup>42</sup> In the reverse anodic scan, the peaks located at 0.46 V, 0.62 V, 0.71 V and 0.78 V are attributed to the reversible de-alloying process, which is in accordance with the previous report.<sup>42</sup> The peak at 1.86 V is assigned to the conversion reaction from Sn to SnS. And the overlapped curves since the 2nd cycle, and the reduction/oxidation peaks located at 0.32/0.46 V, 0.64/0.62 V, and 1.3/1.9 V demonstrate the great reversibility and stability of SnS@C during cycling. The galvanostatic discharge/charge profiles are in accordance with the CV results (Fig. 4c). A long voltage plateau located at ~1.3 V, attributed to the conversion reaction between SnS and Sn, can be observed during the first discharge profile. In the following cycles, the voltage plateau shifts to a higher voltage (~1.4 V).<sup>51</sup> The relative small and multiple voltage plateaus located at 0.68 V and 0.36 V correspond to the alloying process. In the reversible charge profile along with the subsequent cycles, small voltage plateaus centered at ~0.46 V, 0.63 V and 1.90 V are consistent with the anodic peaks in CV files, which are related to the de-alloying process and conversion reaction, respectively. To understand the lithium storage behavior of SnS@C-600 °C, CV curves are also obtained for the first four cycles (Fig. S11†). All these above-mentioned redox peaks in SnS@C can be observed except for the decreased peak intensity compared with that of SnS@C, indicating that SnS@C-600 °C displays the same lithium storage mechanisms, while the electrochemical utilization of the active SnS material is lower than that of SnS@C.

To confirm the cycling stability of SnS@C towards Li-ion storage, long-term cycling behavior is studied at a high current density of 5 A g<sup>-1</sup> (Fig. 4d). The electrode maintains a high reversible capacity of 850.9 mA h g<sup>-1</sup> after 5000 cycles, indicating its superior cycling performance. It shows the same cycling tendency that the capacity decreases in initial cycles and then gradually increases and finally becomes stable in capacity with subsequent cycling compared with that of SnS<sub>2</sub>@C, resulting from the same reason that has been mentioned before in SnS<sub>2</sub>@C. The rate performances (Fig. 4e), in which the current density is increased from 0.1 to 10 A g<sup>-1</sup> and returns to 0.1 A g<sup>-1</sup>, show that it delivers a reversible capacity of 655.3 mA h g<sup>-1</sup> at a high current density of 10 A g<sup>-1</sup>, suggesting the potential high-power application for Li ion storage. It still

maintains a capacity of 1260.5 mA h g<sup>-1</sup> when the current density recovers to 0.1 A g<sup>-1</sup>, indicating the excellent reversibility of SnS@C. Obviously, the SnS@C electrode shows superior cycling stability and rate capability to SnS@C-600 °C (Fig. S12 and S13†). To clarify the electrochemical performances of the SnS@C and SnS@C-600 °C composites, electrochemical impedance spectroscopy (EIS) is further performed (Fig. S14†). The EIS plots consisted of a high-frequency semicircle and an oblique line at the low frequency corresponding to the interface transfer resistance and ion diffusion, respectively. The results show that the SnS@C electrode displays a *R*<sub>ct</sub> value of 185 Ω, which is lower than that of the SnS@C-600 °C electrode (633 Ω), indicating the better kinetics of SnS@C than SnS@C-600 °C. Moreover, it can be noted that the long-term cycling stability and rate capability of the SnS@C electrode are much better than those of the state-of-the-art values for the SnS-based composites reported so far (Fig. 4f and g).<sup>15,25,26,63–69</sup>

Inspired by the above decent LIBs performance of SnS<sub>2</sub>@C nanoplates and SnS@C composites, we are challenged to exploit their potential in the direction of Na<sup>+</sup> storage. As demonstrated in Fig. S15,† severe capacity loss occurs in SnS<sub>2</sub>@C nanoplates, and SnS@C as well as SnS@C-600 °C composites due to the pulverization and structural collapse of the hybrid structure after repeated phase transformation. Hence, we construct hollow rod-like SnS@NC@NG composites derived from MOF precursors to maintain the structural integrity of the electrode during the sodiation/desodiation. As observed in Fig. 1k, the unique structure is deemed to be beneficial for buffering the volume expansion and improving the electrical/ionic diffusion during cycling. Therefore, improved electrochemical behavior toward Na<sup>+</sup> storage for the SnS@NC@NG composites is expected.

The electrochemical performances of SnS@NC@NG as a NIB electrode are investigated in a voltage range of 0.01–3.0 V. Fig. 5a exhibits the cycling performances of SnS@NC@NG at a current density of 100 mA g<sup>-1</sup>. Strikingly, SnS@NC@NG shows stable cycling performances with a high reversible capacity of 723.3 mA h g<sup>-1</sup> and from the third cycles a coulombic efficiency of over 95% can be retained. In contrast, SnS@C exhibits a limited cycle life, which suffers from drastic capacity fading, in which a discharge capacity of 751.2 mA h g<sup>-1</sup> in the 1st cycle drops to 171.3 mA h g<sup>-1</sup> after 100 cycles. In addition, the cycling performance of SnS@NC@NG composites with different NG contents are also investigated, as shown in Fig. S16,† which indicates that the optimal NG content in SnS@NC@NG is 10.8 wt%. Therefore, the following electrochemical characterization is performed for the optimized samples. The CV curve of SnS@NC@NG (Fig. S17†) exhibits three peaks at 1.07 V, 0.58 V and 0.07 V in the first sodiation process. The peak at 1.07 V corresponds to the conversion reaction of SnS into Sn and Na<sub>2</sub>S, and the following two peaks at 0.58 V and 0.07 V are assigned to the multi-step alloying process between Sn and Na.<sup>45</sup> Specially, the reduction peak at 0.58 V is responsible for the formation of SEI films.<sup>18,21</sup> Remarkably, the sharpest peak shifts to large potentials (0.67 V) in the subsequent cycles, and the CV profiles are almost overlapping, indicating the excellent reversibility and cycling stability of

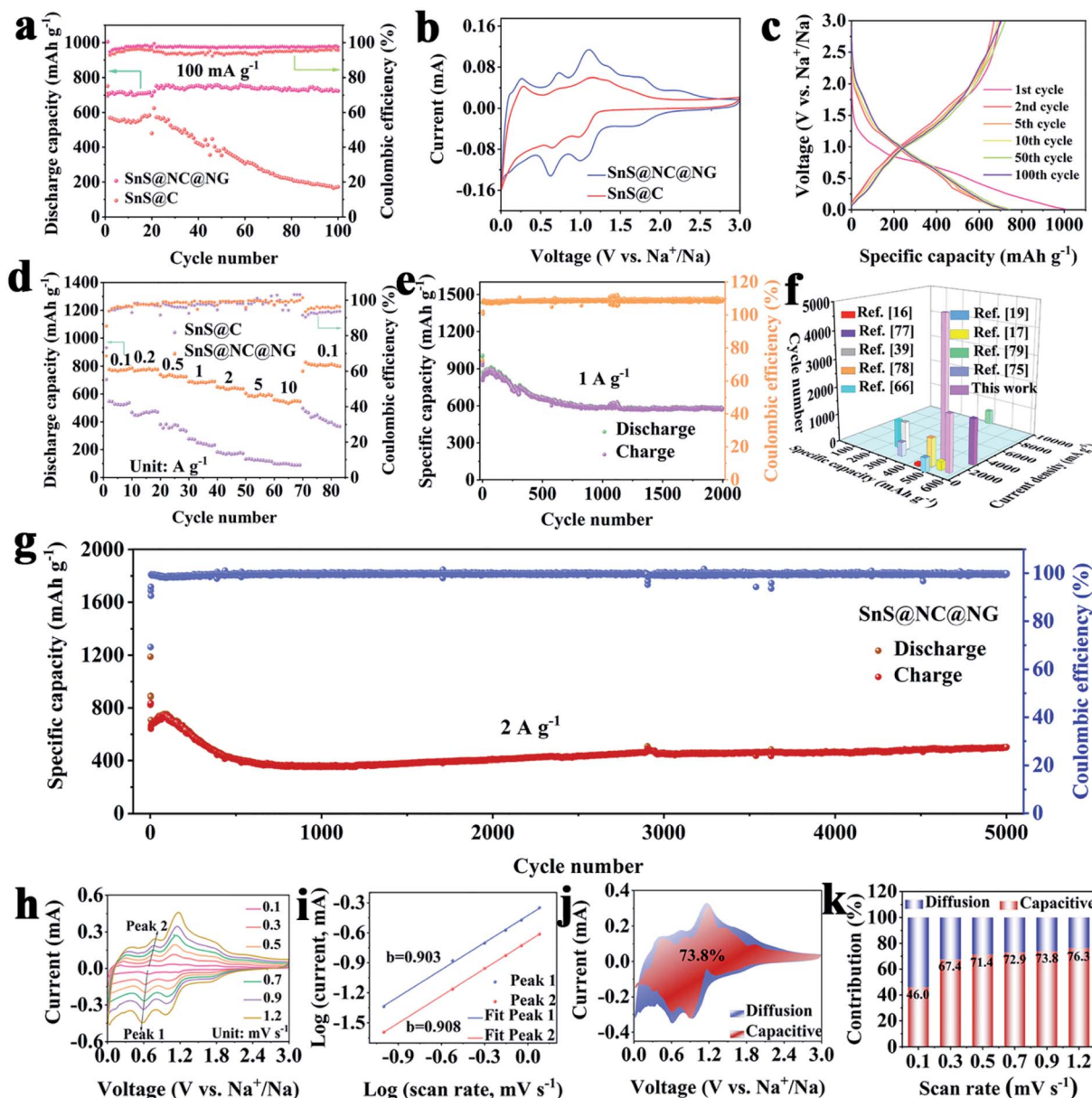


Fig. 5 Electrochemical properties of SnS@NC@NG. (a) Cycling performance of SnS@C and SnS@NC@NG at a current density of  $100 \text{ mA g}^{-1}$ . (b) CV profile comparison of the SnS@C and SnS@NC@NG within the voltage of 0.01–3.0 V (versus  $\text{Na}^+/\text{Na}$ ) at scan rate of  $0.3 \text{ mV s}^{-1}$ . (c) Galvanostatic charge–discharge voltage profiles of the SnS@NC@NG between 0.01 and 3 V at a current density of  $100 \text{ mA g}^{-1}$ . (d) Rate capability of SnS@C and SnS@NC@NG at various current densities from 0.1 to  $10 \text{ A g}^{-1}$ . (e) Long term cycling performance of the SnS@NC@NG at  $1 \text{ A g}^{-1}$ . (f) Comparison of the cycling performance of SnS@NC@NG with that of other reported SnS-based anodes for NIBs. (g) Long-term cycling stability at a high current density of  $2 \text{ A g}^{-1}$  for SnS@NC@NG. (h) CV curves at various scan rate from 0.1 to  $1.2 \text{ mV s}^{-1}$ . (i) The corresponding  $\log(i)$  versus  $\log(v)$  plots. (j) The typical diffusion/capacitive contribution at a scan rate of  $0.9 \text{ mV s}^{-1}$ . (k) The contribution ratio at different scan rates of SnS@NC@NG.

SnS@NC@NG for  $\text{Na}^+$  storage. Of special note, in the first desodiation process, the CV curve of SnS@NC@NG exhibits five sharp peaks at 0.23 V, 0.70 V, 1.1 V, 1.3 V and 1.78 V in the anodic scan. According to the previous studies, the multiple Na–Sn dealloying reaction process of  $\text{Na}_x\text{Sn}$  into Sn can be responsible for the peaks at 0.23 V, 0.7 V and 1.1 V, respectively. The peak at 1.3 V implies the formation of sodium polysulfides and the peak at 1.78 V relates to the reversible conversion reaction.<sup>20,21,70–72</sup> No peak near 2.2 V/1.75 V, which represents

the oxidation/reduction peak of S in the sulfur-containing materials, indicates the stable stability of S in the –C–S–C bond during cycling.<sup>73,74</sup> For SnS@C, the CV curves show a much comparable peak position with SnS@NC@NG except for the worse match from the 2nd cycle to the 4th cycle and the negligible peak at 1.7 V (Fig. S18<sup>†</sup>), suggesting the worse conversion reaction reversibility, which can be responsible for the poor cycling performance. By comparison of the CV profiles of SnS@NC@NG and SnS@C with a similar scan rate of  $0.3 \text{ mV s}^{-1}$

$s^{-1}$  (Fig. 5b), it can be seen that the peak intensity and area of SnS@NC@NG are sharper and larger than those of SnS@C, respectively, indicating the highly available active material (SnS) and high capacity of SnS@NC@NG. On the other hand, smaller polarization can be demonstrated by the smaller potential interval between reduction and oxidation peaks.<sup>70</sup> All of these results clearly demonstrate the enhanced electrochemical kinetics and cycling stability of SnS@NC@NG.

The galvanostatic charge/discharge profiles of SnS@NC@NG evaluated at a current density of 100 mA  $g^{-1}$  within a voltage of 0.01–3.0 V are exhibited in Fig. 5c, which coincidence well with the CV results. A high discharge/charge capacity of 1005.2/697.8 mA h  $g^{-1}$  is delivered in the first cycle with a limited initial coulombic efficiency of 69.4%, which should be attributed to the irreversible formation of the SEI. The subsequent cycles show high reproducibility in the discharge/charge voltage plateaus and specific capacity. Specially, the coulombic efficiency value can reach over 95% from the 3rd cycle, indicating excellent electrochemical performances. Furthermore, the electrochemical behaviors of SnS@NC@NG are tested at the changing current density (Fig. 5d). It shows that the SnS@NC@NG composite delivers discharge/charge capacities of 1087.2/746.3, 786.8/757.0, 740.8/715.8, 688.0/671.4, 652.7/635.0, 605.6/580.6, and 558.0/544.1 mA h  $g^{-1}$  at current densities of 0.1, 0.2, 0.5, 1, 2, 5 and 10 A  $g^{-1}$ , respectively. A high specific capacity of 765.1 mA h  $g^{-1}$  can still be recovered when the current density returns to 0.1 mA  $g^{-1}$ , suggesting good reversibility and stability performance. In sharp contrast, much low capacities are observed in SnS@C for the same current densities, dropping from 704.4 mA h  $g^{-1}$  (0.1 A  $g^{-1}$ ) to 100.0 mA h  $g^{-1}$  (10 A  $g^{-1}$ ). When the current density recovers to 0.1 A  $g^{-1}$ , a low capacity of only 498.2 mA h  $g^{-1}$  is achieved, delivering poor rate capability. EIS is employed to confirm the improved kinetics of SnS@NC@NG. Both Nyquist plots of Fig. S19† consist of a depressed semicircle in medium- and high-frequency regions, as well as an inclined line in low-frequency regions. The equivalent circuit of SnS@NC@NG and SnS@C is given in the inset of Fig. S19.† It is obvious that the SnS@NC@NG displays a much smaller semicircle diameter and more inclined line than SnS@C, which indicate that the SnS@NC@NG has a lower charge-transfer resistance at the interface of the electrode and electrolyte, and a smaller Na<sup>+</sup> diffusion resistance within the electrode. The charge transfer resistance  $R_{ct}$  of SnS@NC@NG is determined to be 324  $\Omega$ , which is much smaller than that of the SnS@C electrode (929  $\Omega$ ), suggesting that the SnS@NC@NG electrode displays an improved electrical conductivity. It is believed that the 3D highly conductive networks and the active materials confined within conductive carbon/graphene are able to facilitate the electron transfer from the SnS throughout the whole electrode, thus showing smaller resistance compared with SnS@C. Furthermore, the long-term cycling of SnS@NC@NG at high current densities of 1 and 2 A  $g^{-1}$  is shown, respectively. It shows that high reversible discharge/charge capacities of 576.3/573.4 mA h  $g^{-1}$  after 2000 cycles at 1 A  $g^{-1}$  and 501.5/499.8 mA h  $g^{-1}$  after 5000 cycles at 2 A  $g^{-1}$  are achieved, respectively (Fig. 5e and g). As for SnS@C (Fig. S15†), it shows

a lower specific capacity than SnS@NC@NG, and there is severe capacity fading resulting in a discharge capacity of only 59.4 mA h  $g^{-1}$  after 500 cycles at 2 A  $g^{-1}$ . Considering the carbon contribution for Na<sup>+</sup> storage, the cycling performances of NC@NG are also tested at a current density of 2 A  $g^{-1}$  (Fig. S20†); the capacity maintains at 129 mA h  $g^{-1}$  after 650 cycles, indicating that the NC@NG only contributes a small amount of capacity to SnS@NC@NG. Moreover, we also test the cycling performance of SnS@NC and SnS@C/rGO (Fig. S21†), respectively. Both samples show low capacity retention after hundreds of cycles. These results fully demonstrate the synergistic effect of PVP and GO towards boosting the sodium storage properties of the SnS@NC@NG composite. To the best of our knowledge, there is no comparable results that can be matched with this superior long-term cycling stability at such high current density (Fig. 5f) and the excellent rate performances (Fig. S22†).<sup>16,17,19,39,66,75–79</sup>

The superior cycling and rate capability are benefited from the remarkable electrochemical kinetics. The CV profiles of SnS@NC@NG with similar shapes are obtained from different sweep rates varying from 0.1 to 1.2 mV  $s^{-1}$  to identify the specific contributions of pseudocapacitive and diffusion effects. Accompanied with the increased scan rate, a slightly shift can be observed from Fig. 5h. A pair of anodic/cathodic peaks (Peak 1/Peak 2, marked by arrows) is used to calculate the relationship between the scan rate and current using eqn (9) and (10):

$$i = av^b \quad (9)$$

$$\log i = b \log v + \log a \quad (10)$$

where  $a$  is a constant;  $i$  and  $v$  represent the peak current and sweep rate, respectively.<sup>80</sup> The  $b$  value can be obtained by the slope of  $\log v - \log i$  plots. Specifically, there is a diffusion-controlled feature when the  $b$ -value is 0.5, whereas the value of  $b$  approaches 1.0, displaying a capacitive process. Fig. 5i gives the plots of  $\log i$  vs.  $\log v$  with a linear fit of two different peaks, Peak 1 and Peak 2, respectively. The  $b$ -values of Peak 1 and Peak 2 are calculated to be 0.903 and 0.908, respectively, indicating that the capacitive- and diffusion-controlled behaviors coexist in the SnS@NC@NG. The quantitative contribution of capacitance can be obtained using eqn (11):

$$i(V) = k_1v + k_2v^{1/2} \quad (11)$$

where  $k_1v$  represents redox capacitive effects, whereas  $k_2v^{1/2}$  displays a diffusion-controlled process, and the calculated value of capacitive contribution is 73.8% at the given scan rate 0.9 mV  $s^{-1}$  (Fig. 5j).<sup>81</sup> Accompanied by the increased scan rate, the redox capacitive contribution rises from 46% to 76.3% (Fig. 5k). The high capacitive contribution can be attributed to the unique structure of SnS@NC@NG, which is beneficial for promoting the charge storage and long-term cycling stability.

To further understand the superior long-term cycling stability in the SnS@NC@NG anode for NIBs, the morphologies of SnS@C and SnS@NC@NG electrodes in different sodiation/disodiation states are investigated by ex situ TEM, as

displayed in Fig. 6a1–b3, respectively. It is obvious that SnS@NC@NG maintains its 3D hollow structures in the fully discharge state after 50 cycles (Fig. 6b2) compared with the fresh SnS@NC@NG (Fig. 6b1), and the 3D conductive structure still maintains integrity even after super long-term cycling (800 cycles at  $2\text{ A g}^{-1}$ ), in which the SnS active materials are confined within hollow NC@NG layers except for SnS inevitably pulverizing into small particles (Fig. 6b3). In comparison, for the cycled SnS@C anode (Fig. 6a2, only after 50 cycles), SnS particles pulverize into smaller nanoparticles (2–4 nm) and some particle clusters aggregate into large particles. Besides, the carbon belts are damaged showing irregular structures. After

long cycling (Fig. 6a3), the morphology of the SnS@C anode is completely damaged, in which the unevenly distributed large particles (>50 nm) with an irregular structure are mixed inhomogeneously with super P and restacked carbon derived from the damaged carbon belt. The SnS@C with limited void space to accommodate the volume change during the sodiation/desodiation should be responsible for significant drastic capacity fading (Fig. 6c1). The superior sodium ion storage behavior of the SnS@NC@NG electrode can be attributed to the compositional and structural benefit from the hybrids, which offers advantages for boosting the  $\text{Na}^+$  storage. Firstly, the 3D interconnected structure with uniform NG coating can provide

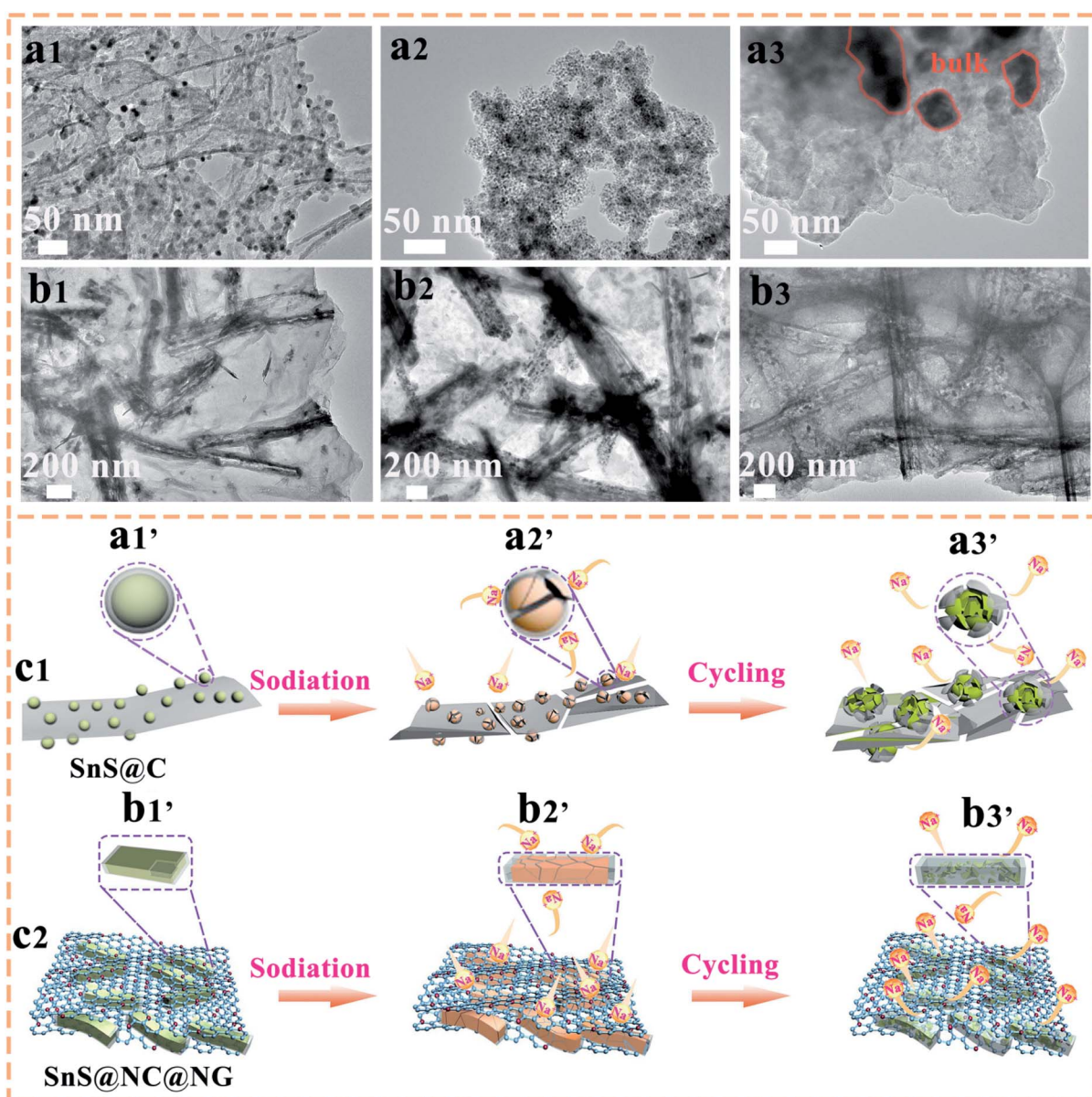


Fig. 6 Schematic illustration of the cycling process of SnS@C and SnS@NC@NG electrodes. TEM images of (a1) fresh SnS@C, (a2) fully discharged SnS@C anode after 50 cycles at  $2\text{ A g}^{-1}$ , and (a3) SnS@C anode after 800 cycles at  $2\text{ A g}^{-1}$ . TEM images of (b1) fresh SnS@NC@NG, (b2) fully discharged SnS@NC@NG anode for NIBs after 50 cycles at  $2\text{ A g}^{-1}$ , and (b3) SnS@NC@NG anode after 800 cycles at  $2\text{ A g}^{-1}$ . (c1 and c2) Schematic illustration of the morphology evolutions of SnS@C and SnS@NC@NG electrodes, respectively (a1', a2' a3', b1', b2' and b3' correspond to a1, a2, a3, b1, b2 and b3, respectively).

a perpetual and continuous electronic conductive network, promoting electron and  $\text{Na}^+$  transport, while preserving the integrity of the electrode structure. Secondly, the hollow rod-like SnS coated with NC could provide adequate internal voids to efficiently accommodate volume expansion, and relax the strain of SnS during the sodiation/desodiation process, which makes the electrode much more robust and stable (Fig. 6c2). Thirdly, the dual coating layer protection prevents active materials SnS from extensive contact with electrolyte, resulting in a stable SEI layer and maintaining the electrochemical activity of the active materials during the long-term cycles. Finally, the N-doped carbon and graphene are both ionically and electronically conducting, resulting in good kinetics for ion/charge transportation. All of these features endow SnS@NC@NG hybrids with an enhanced cycling stability and promoted reaction kinetics for NIBs.

## Conclusions

In summary, we have rationally designed and fabricated novel MOF-derived  $\text{SnS}_2$ @C, SnS@C and SnS@NC@NG composites as advanced electrodes for Li/Na ion storage by a one-step carbonization and sulfidation process. It was demonstrated that the sulfidation temperature has significant influence on the crystal structure between  $\text{SnS}_2$  and SnS. Benefiting from the mono-lamellar structures of  $\text{SnS}_2$ @C nanoplates and SnS@C composites, both of them exhibit outstanding lithium storage properties. We further construct a 3D hollow rod-like SnS@NC@NG anode to accommodate larger  $\text{Na}^+$  by virtue of the synergistic effects of PVP and GO. The suitable hollow structure can effectively alleviate volume expansion and ensure favorable transport kinetics for both electrons and sodium ions during the sodiation/desodiation process, leading to excellent performances for sodium storage in terms of high capacities, stable capacities upon high current densities and ultralong cycles, which surpass those of all previous reported SnS-based electrodes. A combined ex situ TEM analysis proves excellent structural integrity during extensive cycling, accounting for the superior  $\text{Na}^+$  storage behaviors. This work provides a simple and scalable method for efficient construction of high-performance tin sulfide electrodes towards Li and Na ion storage that can be applied in some fast energy storage systems.

## Experimental section

### Synthesis of the Sn-MOF

All the reagents used in the experiment were obtained from commercial sources and used as received. NaOH (0.024 mol) and *o*-phthalic acid (0.012 mol) were dissolved in deionized water (DI) (300 ml) under continuous stirring until a homogeneous solution was formed. Another solution (60 ml) containing  $\text{SnSO}_4$  (0.25 mol) was slowly dropped into the above solution with stirring. The mixed solution was then stirred at 90 °C for 1 h, and stirred for another 6 h at room temperature. The obtained white precipitates were obtained after centrifugation and washed with DI water several times and dried at 60 °C for 12 h.<sup>31</sup>

### Synthesis of $\text{SnS}_2$ @C nanoplates

The as-prepared Sn-MOFs (0.1 g) and sulfur powders (0.5 g) were placed into two ceramic boats separately; the ceramic boats contained sulfur powders were placed in near the gas inlet, and then heated up to 400 °C for 3 h with a heating rate of 2 °C  $\text{min}^{-1}$  under argon gas. After cooling down to room temperature, the product was taken out and its color was found to change from white to yellow.

### Synthesis of SnS@C and SnS@C-600 °C composites

SnS@C and SnS@C-600 °C composites were prepared in a similar process with  $\text{SnS}_2$ @C nanoplates except that the sulfidation temperature was increased from 400 °C to 500 °C or 600 °C, respectively, and the obtained product was black powder.

### Synthesis of SnS@NC@NG, SnS@NC@NG-1, SnS@NC@NG-2 and SnS@NC@NG-3 composites

A transparent solution containing PVP (150 mg) was slowly dropped into a solution containing the MOF (0.2 g) with continuous stirring and ultrasonication for 6 h at room temperature. A certain amount of GO was dispersed in DI (40 ml) to form a uniform solution with ultrasonication and stirring for 5 h. The GO solution then was slowly dropped into the former mixed solution and then stirred for 3 h. Finally, Sn-MOF@PVP@GO was obtained by freeze-drying for 72 h. The SnS@NC@NG with different contents of NG was obtained through a similar sulfuration process to the above route (SnS@C).

### Synthesis of SnS@NC and NC@NG composites

SnS@NC and NC@NG composites were obtained from a similar process of the SnS@NC@NG composite but without adding GO, and the Sn-MOF, respectively.

### Synthesis of SnS@C/rGO composites

SnS@C/rGO composites were obtained from a similar process of the SnS@NC@NG composite but washing PVP out with DI three times before freeze-drying.

### Materials characterization

The crystalline structure of the obtained samples was analyzed by X-ray powder diffraction (XRD, D8 Advance, Bruker AXS) with Cu  $K\alpha$  ( $\lambda = 1.5406$  nm). Raman spectroscopy was characterized using a Horiba Evolution with a laser excitation of 633 nm. Thermogravimetry analysis (TGA, Netzsch STAM 449 F3) was carried out to determine compositions of samples under air with a ramp rate of 10 °C  $\text{min}^{-1}$ . Surface characterization of elemental electronic states was conducted by XPS measurements (PerkinElmer PHI 5000C ESCA). The morphology of the composites was observed using an FE-SEM (JEOL 7500FA, Tokyo, Japan) and Energy-filtered TEM (JEOL 2011 F, Tokyo, Japan).

## Electrochemical measurements

The SnS<sub>2</sub>@C, SnS@C and SnS@NC@NG electrodes were made by pasting slurries containing the active materials (70 wt%), Super P carbon black (20 wt%) and carboxymethyl cellulose (CMC, 10 wt%) on copper foil and dried at 80 °C for 18 h under vacuum. For lithium-ion batteries (LIBs), SnS<sub>2</sub>@C or SnS@C electrodes, along with a polypropylene separator and lithium foil as the counter electrodes are constructed into coin type cells, which were assembled in a glove box under an argon atmosphere (water and oxygen concentration less than 0.1 ppm). The electrolyte was 1 M LiPF<sub>6</sub> salt dissolved in ethylene carbonate (EC)/diethyl carbonate (DEC) in a 1 : 1 volume ratio. For sodium-ion batteries (NIBs), the electrolyte was a mixed solution containing 1 M NaPF<sub>6</sub> in EC/DEC (1 : 1/v/v) and fluoroethylene carbonate (FEC) (5 wt%). Besides, the metallic sodium and glass fiber were used as the counter electrode and the separator, respectively. Electrochemical tests were performed using 2032 coin-type cells. Specifically, the set current density and specific capacity were based on the total mass of the composites. The cycling and rate performances of the coin cells were studied on a LAND battery tester with the voltage range of 0.01–3.0 V at room temperature. Besides, for the long-term cycling performances at high current density (1 A g<sup>-1</sup>, 2 A g<sup>-1</sup> or 5 A g<sup>-1</sup>), all electrodes were first activated for 3 cycles at a current density of 100 mA g<sup>-1</sup> and then tested at high current density for LIBs and NIBs, respectively. Cyclic voltammetry (CV) within the voltage range of 0.01–3.0 V and electrochemical impedance spectroscopy (EIS) in the frequency range of 100 kHz to 0.01 Hz were conducted on an electrochemical workstation (CHI 660E).

## Conflicts of interest

There are no conflicts to declare.

## Acknowledgements

This work was partially supported by the National Key Research and Development Program of China (2017YFA0204600), the National Science Fund for Distinguished Young Scholars (51625102), the National Natural Science Foundation of China (51971065, and 61574039) and the Innovation Program of Shanghai Municipal Education Commission (2019-01-07-00-07-E00028).

## Notes and references

- H. Jin, H. Wang, Z. Qi, D.-S. Bin, T. Zhang, Y. Wang, J. Chen, C. Chuang, Y.-R. Lu, T.-S. Chan, H. Ju, A.-M. Cao, W. Yan, X. Wu, H. Ji and L. J. Wan, *Angew. Chem., Int. Ed.*, 2020, **59**, 2318–2322.
- Z. Wu, G. Liang, W. K. Pang, T. Zhou, Z. Cheng, W. Zhang, Y. Liu, B. Johannessen and Z. Guo, *Adv. Mater.*, 2020, **32**, 1905632.
- D. Larcher and J.-M. Tarascon, *Nat. Chem.*, 2015, **7**, 19–29.
- X. Zhang, S. Guo, P. Liu, Q. Li, S. Xu, Y. Liu, K. Jiang, P. He, M. Chen, P. Wang and H. Zhou, *Adv. Energy Mater.*, 2019, **9**, 1900189.
- Y. Liu, Z. Sun, K. Tan, D. K. Denis, J. Sun, L. Liang, L. Hou and C. Yuan, *J. Mater. Chem. A*, 2019, **7**, 4353–4382.
- H. Yang, L.-W. Chen, F. He, J. Zhang, Y. Feng, L. Zhao, B. Wang, L. He, Q. Zhang and Y. Yu, *Nano Lett.*, 2020, **20**, 758–767.
- Y. Zhao, J. Zhu, S. J. H. Ong, Q. Yao, X. Shi, K. Hou, Z. J. Xu and L. Guan, *Adv. Energy Mater.*, 2018, **8**, 1802565.
- M. Mao, C. Cui, M. Wu, M. Zhang, T. Gao, X. Fan, J. Chen, T. Wang, J. Ma and C. Wang, *Nano Energy*, 2018, **45**, 346–352.
- H. Huang, R. Xu, Y. Feng, S. Zeng, Y. Jiang, H. Wang, W. Luo and Y. Yu, *Adv. Mater.*, 2020, **32**, 1904320.
- X. Liu, Y. Hao, J. Shu, H. M. K. Sari, L. Lin, H. Kou, J. Li, W. Liu, B. Yan, D. Li, J. Zhang and X. Li, *Nano Energy*, 2019, **57**, 414–423.
- G.-M. Weng, Y. Xie, H. Wang, C. Karpocich, J. Lipton, J. Zhu, J. Kong, L. D. Pfefferle and A. D. Taylor, *Angew. Chem., Int. Ed.*, 2019, **131**, 13865–13871.
- J. Liu, Y. Zhang, L. Zhang, F. Xie, A. Vasileff and S.-Z. Qiao, *Adv. Mater.*, 2019, **31**, 1901261.
- Z. Wei, L. Wang, M. Zhuo, W. Ni, H. Wang and J. Ma, *J. Mater. Chem. A*, 2018, **6**, 12185–12214.
- P. Xue, N. Wang, Y. Wang, Y. Zhang, Y. Liu, B. Tang, Z. Bai and S. Dou, *Carbon*, 2018, **134**, 222–231.
- Y. Cheng, Z. Wang, L. Chang, S. Wang, Q. Sun, Z. Yi and L. Wang, *ACS Appl. Mater. Interfaces*, 2020, **12**, 25786–25797.
- S. Wang, Y. Fang, X. Wang and X. W. Lou, *Angew. Chem., Int. Ed.*, 2019, **58**, 760–763.
- C. Zhu, P. Kopold, W. Li, P. A. van Aken, J. Maier and Y. Yu, *Adv. Sci.*, 2015, **2**, 1500200.
- B. Qu, C. Ma, G. Li, C. Xu, J. Xu, Y. S. Meng, T. Wang and J. Y. Lee, *Adv. Mater.*, 2014, **26**, 3854–3859.
- J. Zhao, G. Wang, R. Hu, K. Zhu, K. Cheng, K. Ye, D. Cao and Z. Fan, *J. Mater. Chem. A*, 2019, **7**, 4047–4054.
- D. Chao, C. Zhu, P. Yang, X. Xia, J. Liu, J. Wang, X. Fan, S. V. Savilov, J. Lin, H. J. Fan and Z. X. Shen, *Nat. Commun.*, 2016, **7**, 12122.
- T. Zhou, W. K. Pang, C. Zhang, J. Yang, Z. Chen, H. K. Liu and Z. Guo, *ACS Nano*, 2014, **8**, 8323–8333.
- P. K. Dutta, U. K. Sen and S. Mitra, *RSC Adv.*, 2014, **4**, 43155–43159.
- Y. Li, J. P. Tu, H. M. Wu, Y. F. Yuan and D. Q. Shi, *Mater. Sci. Eng., B*, 2006, **128**, 75–79.
- L. Wu, H. Lu, L. Xiao, X. Ai, H. Yang and Y. Cao, *J. Power Sources*, 2015, **293**, 784–789.
- J. Xia, L. Liu, S. Jamil, J. Xie, H. Yan, Y. Yuan, Y. Zhang, S. Nie, J. Pan, X. Wang and G. Cao, *Energy Storage Mater.*, 2019, **17**, 1–11.
- S. Zhang, G. Wang, Z. Zhang, B. Wang, J. Bai and H. Wang, *Small*, 2019, **15**, 1900565.
- Z. Chen, R. Wu, H. Wang, Y. Jiang, L. Jin, Y. Guo, Y. Song, F. Fang and D. Sun, *Chem. Eng. J.*, 2017, **326**, 680–690.
- P. Wang, M. Shen, H. Zhou, C. Meng and A. Yuan, *Small*, 2019, **15**, 1903522.

- 29 X. Xu, J. Liu, J. Liu, L. Ouyang, R. Hu, H. Wang, L. Yang and M. Zhu, *Adv. Funct. Mater.*, 2018, **28**, 1707573.
- 30 H. Chen, L. Shi, X. Liang, L. Wang, T. Asefa and X. Zou, *Angew. Chem., Int. Ed.*, 2020, **132**, 19822–19826.
- 31 X. Zhou, S. Chen, J. Yang, T. Bai, Y. Ren and H. Tian, *ACS Appl. Mater. Interfaces*, 2017, **9**, 14309–14318.
- 32 P. A. Fernandes, M. G. Sousa, P. M. P. Salomé, J. P. Leitão and A. F. da Cunha, *CrystEngComm*, 2013, **15**, 10278.
- 33 W. Tian, H. Hu, Y. Wang, P. Li, J. Liu, J. Liu, X. Wang, X. Xu, Z. Li, Q. Zhao, H. Ning, W. Wu and M. Wu, *ACS Nano*, 2018, **12**, 1990–2000.
- 34 W. Li, J. Qian, T. Zhao, Y. Ye, Y. Xing, Y. Huang, L. Wei, N. Zhang, N. Chen, L. Li, F. Wu and R. Chen, *Adv. Sci.*, 2019, **6**, 1802362.
- 35 S. Liu, L. Sun, F. Xu, J. Zhang, C. Jiao, F. Li, Z. Li, S. Wang, Z. Wang, X. Jiang, H. Zhou, L. Yang and C. Schick, *Energy Environ. Sci.*, 2013, **6**, 818–823.
- 36 D. Ji, L. Fan, L. Tao, Y. Sun, M. Li, G. Yang, T. Q. Tran, S. Ramakrishna and S. Guo, *Angew. Chem., Int. Ed.*, 2019, **58**, 13840–13844.
- 37 H. X. Zhong, J. Wang, Y. W. Zhang, W. L. Xu, W. Xing, D. Xu, Y. F. Zhang and X. B. Zhang, *Angew. Chem., Int. Ed.*, 2014, **53**, 14235–14239.
- 38 M. Wang, H. Xu, Z. Yang, H. Yang, A. Peng, J. Zhang, J. Chen, Y. Huang, X. Li and G. Cao, *ACS Appl. Mater. Interfaces*, 2019, **11**, 41363–41373.
- 39 X. Xiong, C. Yang, G. Wang, Y. Lin, X. Ou, J.-H. Wang, B. Zhao, M. Liu, Z. Lin and K. Huang, *Energy Environ. Sci.*, 2017, **10**, 1757–1763.
- 40 C. Wang, K. Tang, Q. Yang and Y. Qian, *Chem. Phys. Lett.*, 2002, **357**, 371–375.
- 41 B. Luo, Y. Fang, B. Wang, J. Zhou, H. Song and L. Zhi, *Energy Environ. Sci.*, 2012, **5**, 5226–5230.
- 42 G. Li, J. Sun, W. Hou, S. Jiang, Y. Huang and J. Geng, *Nat. Commun.*, 2016, **7**, 10601.
- 43 J. Li, S. Han, C. Zhang, W. Wei, M. Gu and L. Meng, *ACS Appl. Mater. Interfaces*, 2019, **11**, 22314–22322.
- 44 S. Gao, L. Yang, Z. Liu, J. Shao, Q. Qu, M. Hossain, Y. Wu, P. Adelhelm and R. Holze, *Energy Technol.*, 2020, **8**, 2000258.
- 45 Y. Zhang, N. Wang, Z. Lu, P. Xue, Y. Liu, Y. Zhai, B. Tang, M. Guo, L. Qin and Z. Bai, *Electrochim. Acta*, 2019, **296**, 891–900.
- 46 J.-G. Wang, H. Sun, H. Liu, D. Jin, X. Liu, X. Li and F. Kang, *ACS Appl. Mater. Interfaces*, 2018, **10**, 13581–13587.
- 47 Y. Liu, Z. Sun, X. Sun, Y. Lin, K. Tan, J. Sun, L. Liang, L. Hou and C. Yuan, *Angew. Chem., Int. Ed.*, 2020, **59**, 2473–2482.
- 48 X. Jin, H. Huang, A. Wu, S. Gao, M. Lei, J. Zhao, X. Gao and G. Cao, *ACS Nano*, 2018, **12**, 8037–8047.
- 49 J. Xia, L. Liu, J. Xie, H. Yan, Y. Yuan, M. Chen, C. Huang, Y. Zhang, S. Nie and X. Wang, *Electrochim. Acta*, 2018, **269**, 452–461.
- 50 Q. Zhang, R. Li, M. Zhang, B. Zhang and X. Gou, *Electrochim. Acta*, 2014, **115**, 425–433.
- 51 M. Choi, W. William, J. Hwang, D. Yoon and J. Kim, *J. Ind. Eng. Chem.*, 2018, **59**, 160–168.
- 52 Y. Du, Z. Yin, X. Rui, Z. Zeng, X.-J. Wu, J. Liu, Y. Zhu, J. Zhu, X. Huang, Q. Yan and H. Zhang, *Nanoscale*, 2013, **5**, 1456–1459.
- 53 D. Guan, L. Ma, D. Pan, J. Li, X. Gao, Y. Xie, M. Qiu and C. Yuan, *Electrochim. Acta*, 2017, **242**, 117–124.
- 54 T.-J. Kim, C. Kim, D. Son, M. Choi and B. Park, *J. Power Sources*, 2007, **167**, 529–535.
- 55 H. Sun, G. Xin, T. Hu, M. Yu, D. Shao, X. Sun and J. Lian, *Nat. Commun.*, 2014, **5**, 4526.
- 56 L. Wu, J. Zheng, L. Wang, X. Xiong, Y. Shao, G. Wang, J.-H. Wang, S. Zhong and M. Wu, *Angew. Chem., Int. Ed.*, 2019, **58**, 811–815.
- 57 S. Huang, M. Wang, P. Jia, B. Wang, J. Zhang and Y. Zhao, *Energy Storage Mater.*, 2019, **20**, 225–233.
- 58 D. Cheng, L. Yang, J. Liu, R. Hu, J. Liu, K. Pei, M. Zhu and R. Che, *J. Mater. Chem. A*, 2019, **7**, 15320–15332.
- 59 D. Gao, Y. Wang, Y. Liu, H. Sun, M. Wu and H. Zhang, *J. Colloid Interface Sci.*, 2019, **538**, 116–124.
- 60 Y. Wang, J. Zhou, J. Wu, F. Chen, P. Li, N. Han, W. Huang, Y. Liu, H. Ye, F. Zhao and Y. Li, *J. Mater. Chem. A*, 2017, **5**, 25618–25624.
- 61 Y. Zuo, X. Xu, C. Zhang, J. Li, R. Du, X. Wang, X. Han, J. Arbiol, J. Llorca, J. Liu and A. Cabot, *Electrochim. Acta*, 2020, **349**, 136369.
- 62 H.-E. Wang, X. Zhao, X. Li, Z. Wang, C. Liu, Z. Lu, W. Zhang and G. Cao, *J. Mater. Chem. A*, 2017, **5**, 25056–25063.
- 63 Q. Pan, F. Zheng, Y. Wu, X. Ou, C. Yang, X. Xiong and M. Liu, *J. Mater. Chem. A*, 2018, **6**, 592–598.
- 64 Q. Lian, G. Zhou, J. Liu, C. Wu, W. Wei, L. Chen and C. Li, *J. Power Sources*, 2017, **366**, 1–8.
- 65 Q. Lian, G. Zhou, X. Zeng, C. Wu, Y. Wei, C. Cui, W. Wei, L. Chen and C. Li, *ACS Appl. Mater. Interfaces*, 2016, **8**, 30256–30263.
- 66 Y. Zhang, P. Wang, Y. Yin, X. Zhang, L. Fan, N. Zhang and K. Sun, *Chem. Eng. J.*, 2019, **356**, 1042–1051.
- 67 Y. Zhou, Q. Wang, X. Zhu and F. Jiang, *Nanomaterials*, 2018, **8**, 135.
- 68 Y. Zhang, H. Sun, C. Wang, D. Yang, Y. Li, W. Zhang, H. Wang, J. Zhang and D. Li, *Nanoscale*, 2019, **11**, 12846–12852.
- 69 J. Liu, M. Gu, L. Ouyang, H. Wang, L. Yang and M. Zhu, *ACS Appl. Mater. Interfaces*, 2016, **8**, 8502–8510.
- 70 L. Wang, X. Li, Z. Jin, Z. Liang, X. Peng, X. Ren, B. Gao, G. Feng, P. K. Chu and K. Huo, *J. Mater. Chem. A*, 2019, **7**, 27475–27483.
- 71 E. Cho, K. Song, M. H. Park, K.-W. Nam and Y.-M. Kang, *Small*, 2016, **12**, 2510–2517.
- 72 X. Zhou, Y. Zhong, M. Yang, M. Hu, J. Wei and Z. Zhou, *Chem. Commun.*, 2014, **50**, 12888–12891.
- 73 J. Yang, X. Zhou, D. Wu, X. Zhao and Z. Zhou, *Adv. Mater.*, 2017, **29**, 1604108.
- 74 S. Xin, Y.-X. Yin, Y.-G. Guo and L.-J. Wan, *Adv. Mater.*, 2014, **26**, 1261–1265.
- 75 Y. Wang, Y. Zhang, J. Shi, X. Kong, X. Cao, S. Liang, G. Cao and A. Pan, *Energy Storage Mater.*, 2019, **18**, 366–374.
- 76 T. Ma, L. Sun, Q. Niu, Y. Xu, K. Zhu, X. Liu, X. Guo and J. Zhang, *Electrochim. Acta*, 2019, **300**, 131–137.

- 77 D. Chao, B. Ouyang, P. Liang, T. T. T. Huong, G. Jia, H. Huang, X. Xia, R. S. Rawat and H. J. Fan, *Adv. Mater.*, 2018, **30**, 1804833.
- 78 X. Hu, J. Chen, G. Zeng, J. Jia, P. Cai, G. Chai and Z. Wen, *J. Mater. Chem. A*, 2017, **5**, 23460–23470.
- 79 M. Hu, H. Zhang, L. Yang and R. Lv, *Carbon*, 2019, **143**, 21–29.
- 80 T. H. T. Luu, D. L. Duong, T. H. Lee, D. T. Pham, R. Sahoo, G. Han, Y.-M. Kim and Y. H. Lee, *J. Mater. Chem. A*, 2020, **8**, 7861–7869.
- 81 J. Sheng, L. Yang, Y.-E. Zhu, F. Li, Y. Zhang and Z. Zhou, *J. Mater. Chem. A*, 2017, **5**, 19745–19751.